Magnetotelluric Well Stimulation Monitoring in the Cooper Basin, South Australia

Thesis submitted in accordance with the requirements of the University of Adelaide for an Honours Degree in Geophysics.

Oliver William Putland

July 2014

ABSTRACT

Hydraulic stimulation tactics allow for the economical extraction of tight-gas plays by increasing the hydraulic conductivity of impermeable formations. The rise of shale-gas exploration and production has seen the implementation of horizontal drilling to pump pressurised fluids into a formation, reactivating paleo-fracture networks from induced pressure instability. The fracture networks stimulate: reduction in pore pressure, increasing pore connectivity and provides new paths for hydrocarbon migration. Deep geophysical monitoring is required to analyse the geological impacts from hydraulic fracturing (fracking), they also aid to increase well success rates. Microseismic surveying is currently the only technique employed to monitor these induced effects, however passive seismic monitoring is not directly sensitive to the physical properties of formation fluids.

In Australia's Cooper Basin a hydraulic fracturing procedure has been monitored using the electromagnetic technique magnetotellurics. Electromagnetism is highly sensitive to subsurface fluid properties and those impacting flow rates, magnetotellurics aims to map the temporal and spatial fluid dynamics of the injection. The proposed outcomes are to monitor temporal changes the injected fracture fluids cause to regional electromagnetic distortions. Distortion analysis is used to describe the geoelectric strike, to infer fluid-flow. Magnetotelluric inverse modelling aims to constrain spatial regions of induced resistivity changes. Temporal fluid percolation properties can then be related to the migration of bulk-fluid movement and also regions of accumulations, highlighting potential stratigraphic traps.

This report describes early-stage feasibility evaluation monitoring the hydrogeological changes induced from hydraulic fracturing at 3000 m depths. This study presents the findings from phase tensor dimensionality and inverse modelling in two dimensions

of a 12 hour recording prior to injection and another recording posterior to fracking. Current data quality is below conclusive standards, particularly in the dead-band (5 - 20 seconds). The regional low resistivity estimates from the Cooper Basin correlate to injection distortion depths within the dead-band, reducing the likelihood of small error margins for depths of interest. Inverse models show sensitivity to the spatial changes at 3000 m depth, showing a 300 m vertical dispersion of fluids at one station. If station and daily resistivity error estimates are enhanced, particularly in the dead-band, and if they follow the same trend as the highest-quality station's modelled temporal changes the changes could be monitored. At this stage, this report provides the background for the on going study attempting to resolve these changes.

KEYWORDS

Magnetotelluric, Resistivity, Monitoring, Dimensionality, Phase-Tensor, Distortion

Table of Contents

List of Figures

INTRODUCTION

Onshore shale gas extraction has seen an explosion of interest in the past few years with large global reserves potentially providing a vast majority of the population with electricity (Cipolla et al., 2010). However with interest comes contention, based upon the potential and current environmental impacts of shale gas production, namely gas-leakage and waste-loss into aquifer systems (Bierman et al., 2011). Shale formations and other tight-gas formations inhibit fluid migration due to the high capillary pressures between grains of impermeable sequences relative to adjacent more permeable sedimentary facies (Mandl & Harkness, 1987). Tight-gas plays have seen the implementation of horizontal steam-injections catalysing hydraulic fracturing (fracking) in formations to stimulate economic hydraulic conductivity rates (Cipolla et al., 2010).

Geophysical monitoring of induced well-production has predominantly been interpreted from microseismic surveying, measuring induced well microseismicity to infer velocity models representing reservoir geomechanical and inelastic deformation (Maxwell et al., 2010). Microseismic inversions of hydraulic-fracture stimulations are highly dependent upon the velocity models used, resulting in poor depth resolution of fracture planes (Mandl & Harkness, 1987). To overcome this defect two-separately located geophone arrays, surface and down-hole, are required to effectively map the spatial characteristics of fracking (Maxwell, 2014). Joint inversion of these techniques allow for temporal and spatial illustrations of hydraulic fracture migration (and orientation) to which fluid migration is indirectly inferred (Du et al., 2008). Dense fracture networks are associated to high fluid flow, highlighting regions for potential wells. Seismicity is not directly sensitive to the physical properties of the injected fluids - hence its provides for indirect inferences of potential hydraulic conductivity rates (Eisner et al., 2010).

Archie's Law proposes: 'fluids travelling through a porous sedimentary rock will conduct electrical current at a rate dependent on the porosity and ionic saturation of the fluid within the rock' (Archie, 1942). Therefore the introduction of ionic fluids to the subsurface could potentially be mapped from electrical resistivity surveying. A recent report (Peacock et al., 2013) refers to analysing magnetotelluric signals to determine phase tensor elliptical properties and infer galvanic dimensionality. Providing the most effective means of monitoring temporal changes in a stimulated enhanced geothermal system (EGS) in Paralana, South Australia. The mapped resistivity models in conjunction with surface microseismic mapping could be used to implicate: fracture orientation and migration, fluid migration and hydraulic conductivity. Furthermore depth constraints can be provided in regions of minimal static-distortions, relegating the need for down hole microseismics. The importance of these implications could provide for effective gas and waste recovery whilst also ameliorating monitoring and environmental costs of down-hole surveying.

This study provides the procedural steps and early-stage feasibility analysis of magnetotelluric (MT) impedances to determine the dimensions of induced distortions in the Cooper Basin, South Australia: Figure 1. The experiment deployed 40 proximal MT stations processed within bandwidths 0.01 Hz - 100 Hz, in the attempt to recover high-resolution resistivity changes from hydraulic fracturing in the Roseneath Shale and underlying formations, Figure 2. The aim is to determine the dimensionality and depth-dependent resistivity changes associated with ten-stage fracking at 3000 m depth. The results of which can be attributed to the temporal and spatial fluid dynamics and further related to the geological impacts. Presently only one station has shown sensitivity to the injected fluids. Further development of the study will ascertain the true limitations of this innovative technique.

BACKGROUND

Structural Setting

In order of succession the Warburton, Cooper and Eromanga Basins underlie the Lake Eyre Basin located in the north-east margin of South Australia, Figure 2. Geological well and seismic analysis of the area suggest the region experienced fluctuations in regional extension throughout the Permian. A shift to a compressional stress regime progressed shortly after (Sun, 1997) (Mavromatidis, 2008). The underlying geometry of the Warburton Basin has been imposed on successive basin-morphologies. The Alice-Springs orogeny produced granitic intrusives enriched in radiogenic material through the crust to deform the Warburton Basin, extensive regional imbricate thrust faulting is apparent (Meixner & Holgate, 2009; Apak, 1994).

Reactivation of N-E trending thrust faults created lead to topographical ridges within the region, nucleating the topographical margins of Cooper Basin deposition (Apak, 1994). Three major troughs formed either side, developing into the three major sedimentary depocentres in the region; Patchawarra, Nappamerri and Tenappera (Ahmad, 2014). Glaciation in the Late Permian, eroded the upper-layers of the Warburton Basin, an unconformity to which phased into the presently known Cooper Basin (Alexander et al., 1996). Post-glacial depositional episodes of intermittent high sediment accumulation and cessation occurred throughout the Late Triasssic, episodes of transgressive and regressive eustacy and the eventual break to a non-marine fluvial deposition. The Nappamerri region has been the focus of natural-gas production in the Cooper Basin for many decades now. The region has experienced tectonic quiescence since, early Eromanga deposition. The Eromanga and Lake Eyre Basins reflect this showing horizontal bedding of mostly non-marine sedimentary deposition. Recent stress analysis has

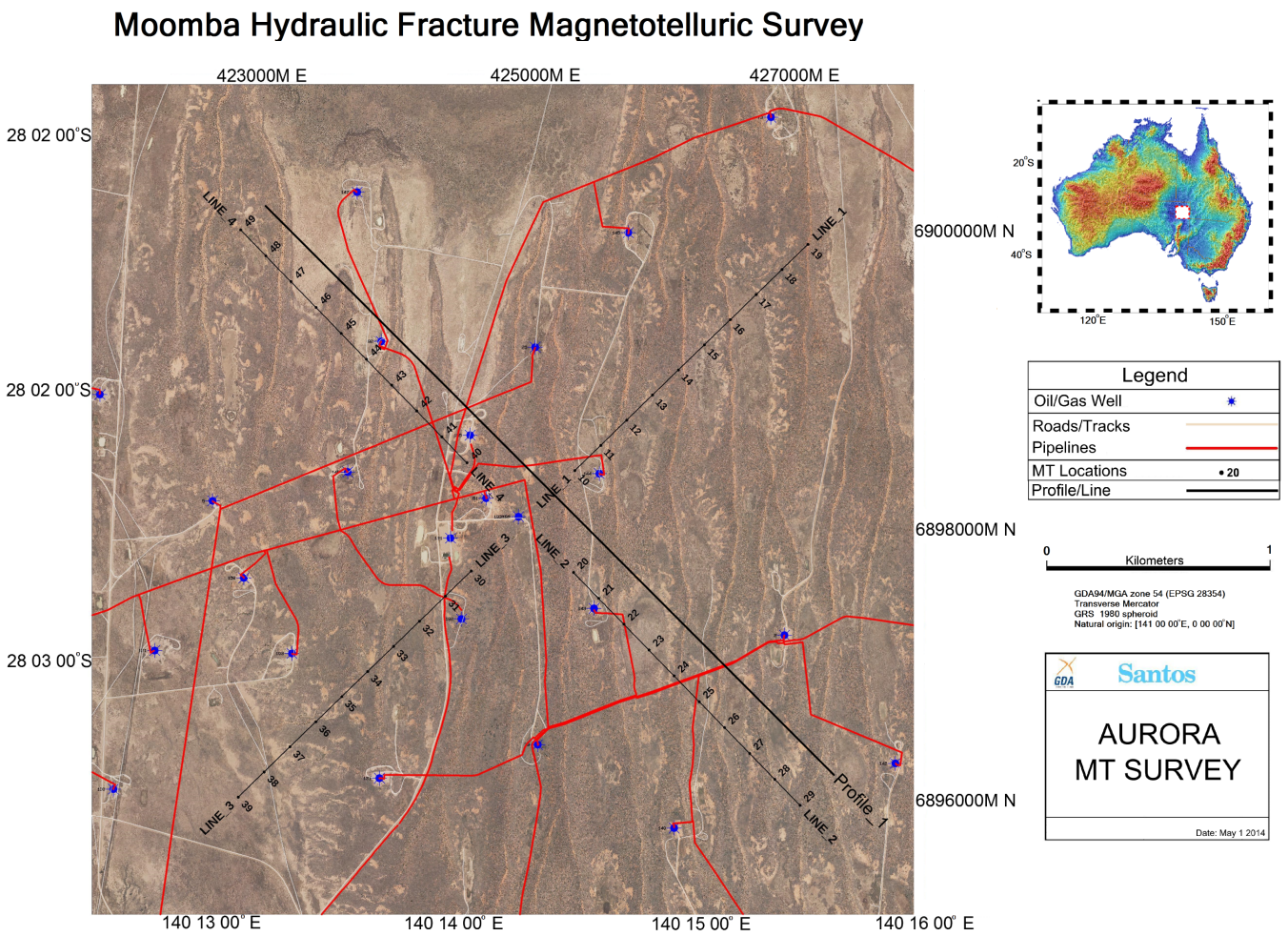

Figure 1: Aerial photograph of Moomba Gas Facility in South Australia. The photograph shows forty magnetotelluric stations along four separate lines trending north east and south west. Stations are separated by 200 m. The profile line shows the transect within this report. Gas pipelines and major oil or gas wells are densely populated and can attribute to MT noise. Moomba Gas Facility lies within a longitudinal dunal system. The top right figure shows a digital elevation model of Australia and Moombas location in inland Australia. Aerial photograph from AURORA ENERGY, SANTOS, A. White, 2011. Digital Elevation Model, Geoscience Australia, 2001.

shown that the stress environment is typified by strike-slip or normal faulting stress, depth-dependent. Present day stress below 3 km is characterised by strike-slip focal mechanisms and today heat flow is on average 100 mW/m^3, corresponding to a geothermal gradient of 40^o / km (Beardsmore, 2004). The high geothermal gradient is suspected from erosion of the radiogenic intrusive (Hillis et al., 1998).

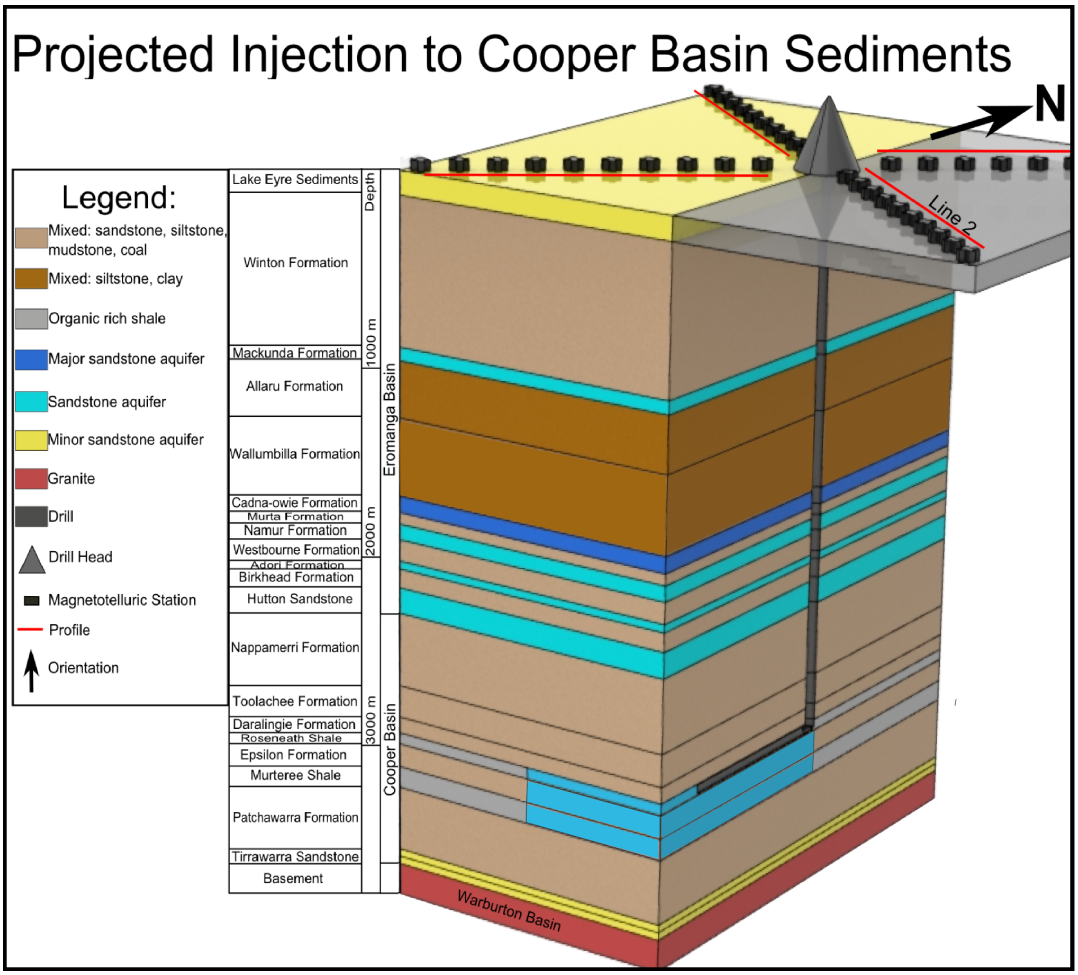

Figure 2: Stratigraphic sequences of the Cooper-Eromanga Basins. Cross section through the middle visualises the drilling and likely fracture pathways given the principle stresses are likely vertical (Pitkin et al., 2012). The surface shows the station set-up relative to injection bore. The drill is shown to be located within the thin Roseneath shale at approximately 3000 m depth. Stratigraphic sequence is a three-dimensional ideation from PIRSA website.

Cooper Basin Lithology

The oldest sedimentary units in the basin were deposited in the Late Carboniferous to Early Permian. These units are expressed as the Merrimelia Formation and Tirrawarra Sandstone units in Figure 2, with sedimentary features characteristic of glaciofluvial environment (Apak, 1994). These sediments are flat-lying due to glacial abrasion of basement bedding (Alexander et al., 1996). Global warming led to glacial regression at the turn of Permian, with till dropstones present in later Tirrawarra units (Krawczynski, 2004). Landscape acclimation to thermal subsidence, led to floodplain, peat swamp and highly sinuous fluvial environments. The overlying Patchawarra formation is described as an upward fining sandstone embedded with laterally extensive siltstone, mudstone, coal and a potential hydrocarbon source (Alexander et al., 1996).

Overlying the Patchawarra formation, lie two separated shale formations with the injection lying within these units. Further subsidence of the Cooper Basin lead to a depression near-base topographic relief and a depositional influx of lacustrine sediments (Alexander et al., 1996). The Murteree Shale is characterised by fine-grained sandstone of predominantly argillaceous siltstone, interpreted as a lacustrine environment (Alexander et al., 1996). Changes to the landscape lead to the deposition of the Epsilon Formation, containing poorly sorted sandstone clasts and localised regions of dense siltstone, mudstone and coal laminates, proposing a fluvio-deltaic depositional model. The basin then proceeded to undergo geological deja vu, experiencing the same sequence of environmental evolution once more with the Roseneath (lacustrine) and Daralingie (fluvio-deltaic) sediments expressing these units. Shale core sample held significant amounts of clay content, as high as 50 % split into kaolinite, illite and siderite (Ahmad, 2014). Pyrite is also contained within the formations, X-ray diffraction shows limits as high as 0.04%. Pore gas has been characterised as terrestrial in origin with log-

sampled gas suggesting a primary composition of type II kerogen (Alexander et al., 1996). Thermal maturation of hydrocarbons forming economical gas content is likely from overburden pressures and the thermal conduction from hot intrusive granodioritic material (Beardsmore, 2004). The Roseneath Shale is the target of introduced injection with high-gas content inferred from the elevated hydrostatic pressures and core-samples (Khaksar & Mitchell, 1995; Krawczynski, 2004).

Hydraulic Fracturing Procedure

Vertical drilling took place at the centre of the profile with horizontal drilling extending 1000 m south approximately parallel to the surface. Fluid-injections began on the 29th of March with spatial and temporal sectioning of fluid pumping lasting twelve days. Pumping was for a 10-phase regime beginning at the distal edge of surface drilling location proceeding north. Pumping ceased twelve days later marking the beginning of the fluid drawback phase. Geophysical surveying from SANTOS suggests fracture deformation is restricted to the Roseneath, Epsilon and Murteree formations with hydraulic conductivities of 1.5 mmscf per day recorded at Moomba Well-193 (Santos, 2014). For more information on hydraulic fracturing, see (Hubbert & Willis, 1972; Valko & Economides, 1995).

MAGNETOTELLURIC THEORY

Our Earth's geomagnetic field fluctuates from processes involving solar radiation and currents in the Earth's magnetosphere (Chave & Jones, 2012). Climatic and solar fluctuations create a resonance in the magnetosphere, conducting the event globally. Localised lightning for example, creates high-frequency electromagnetic distortions that are transmitted globally (Simpson & Bahr, 2005). Reaching solid Earth, heterogeneities of electrical mediums diversify the energy of an incident electromagnetic waves. Magne-

totelluric's passively exploits this naturally occurring phenomena by recording geomagnetic variations of the time-varying electric ($\vec{E}$) and magnetic ($\vec{H}$) fields at the surface. The frequency components of the measured fields are indicative of the electrical properties of the medium. Rikitake (1949) and Tikhonov (1951) first described the possibility to exploit this naturally occurring phenomenon, with Cagniard (1953) providing the first theoretical concepts accommodating its geophysical application. Further research expanded Cagniard's (1953) half-space model and has lead to the developments and diversification of magnetotelluric applications.

Recording instruments are typically orientated to align with the principal components of geomagnetic variation strike (N-S, E-W). This can be realigned to geoelectric strike with the naming convention transverse electric mode (TE) and the orthogonal transverse magnetic mode (TM). With TE mode measuring the effects of a latitudinally propagating magnetic wave and TM measuring the longitudinal (Simpson & Bahr, 2005). Comparison of the induced orthogonal electric and magnetic fields are estimated from the transfer function Equation (3) relating electrical field changes in respect to the magnetic field change. The electric field strength $\vec{E}$ and magnetic induction $\vec{B}$ ($\vec{B} = \frac{\vec{H}}{\mu_0}$, μ_0 is the magnetic permeability of free space),

$$\vec{E} = \Delta\vec{U} \cdot d^{-1}; \qquad \text{Potential Field Strength}(Vm^{-1}) \tag{1}$$

are independently processed and then applied to Maxwell's fundamental equations which describe the behavioural properties of orthogonal electric and magnetic time-varying fields (Chave & Jones, 2012). These are then related to a set of diffusive equations

describing the behaviour of a vertically propagating magnetic field ($\frac{dH}{dt}$) or electric field ($\frac{dE}{dt}$) to the rate of change of the converse field (Booker, 2014).

$$\nabla^2 \vec{E} = \mu\sigma \frac{d\vec{E}}{dt}; \qquad \nabla^2 \vec{H} = \mu\sigma \frac{d\vec{H}}{dt} \tag{2}$$

where the rate of change of natural Earth tellurics is dependent upon geological inhomogeneities and alterations to these gradients (Cagniard, 1953). An assumption that electrical displacement currents are negligible ($\sigma >> \omega\epsilon$), simplifying and removing the secondary term (not present above) reflecting secondary field distortions (Jiracek, 1990). Subjected to Fourier Transform space, these result in the Helmholtz equation relating the time domain to the frequency domain. Solution to the Helmholtz equation requires a secondary Fourier Transform for resolving the impedance estimates (Parker, 1994; Chave & Jones, 2012).

The magnetotelluric impedance tensor $\vec{Z_{ij}}$ is defined dependent on angular frequency (ω),

$$\begin{bmatrix} \vec{E_x}(\omega) \\ \vec{E_y}(\omega) \end{bmatrix} = \begin{bmatrix} \vec{Z_{xx}}(\omega) & \vec{Z_{xy}}(\omega) \\ \vec{Z_{yx}}(\omega) & \vec{Z_{yy}}(\omega) \end{bmatrix} \cdot \begin{bmatrix} \frac{\vec{B_x}(\omega)}{\mu_0} \\ \frac{\vec{B_y}(\omega)}{\mu_0} \end{bmatrix} \tag{3}$$

describes transformations of the electromagnetic waves propagating through an anisotropic-medium. It relates a rock to its ability to resist electrical flow (resistivity) from the induction of a time-varying electromagnetic field.

Typically resistivity (ρ, Ω m) measurements are used to describe the geological induction characteristics of a wavelength. The reciprocal of resistivity is conductivity (σ, $S\ m^{-1}$), the two are interchangeable in descriptive electromagnetism (Simpson &

Bahr, 2005). Extracted from the complex tensor are individual impedance estimates from the transfer function, eg.

$$\vec{Z_{xy}} = \frac{\vec{E_x}}{\vec{B_y}} \tag{4}$$

to which further diagnostics can be formulated. The skin depth δ defines the depth margin to which attenuation of wave energy approaches $\frac{1}{e}$,

$$\delta = \quad \delta = \sqrt{\frac{2}{\omega\mu_0\sigma}}; \qquad \textbf{or} \qquad \delta = 500\sqrt{\rho T} \tag{5}$$

and is recognised as a proxy to layer-depth, where T is the period in seconds (Cagniard, 1953). Differentiation of resistivity layers and accumulative skin depths is the basis of inverse modelling. Apparent resistivity (ρ_a) of the bulk-medium,

$$\rho_a = \frac{1}{\omega\mu_0}|\vec{Z}|^2 \tag{6}$$

describes the average conductive content of heterogeneous mediums. The phase between transfer function component's orthogonal fields,

$$\vec{\Phi_{ij}} = \arctan\frac{\Im(\vec{Z_{ij}})}{\Re(\vec{Z_{ij}})} \tag{7}$$

describe the relative layer-changes of electrical induction.

Electronic induction of geological bodies are dependent upon the bulk-resistivity of the volume influencing a propagating wave and is termed the apparent resistivity. In general most minerals act to resist induction, however minor phases of highly conductive content increase the impact of bulk-conductivity dramatically. Some of the known crustal conductive phases are: partial melts, water, salinity, clay minerals, carbon dioxide, graphite and sulphides (Palacky & West, 1991; Nesbitt, 1993). Decomposition of the

impedance tensor's four components are defined by rotational invariants, to which inform the user of the dimensional properties of regional and localised distortions (Groom & Bahr, 1992; Weaver et al., 2006; Marti et al., 2009).

In sedimentary rocks the resistivity of a rock at constant pressure and depth conditions is described by Archie's equation (1942),

$$\rho_o = a\varphi^{-m} S_w^{-n} \rho_w \tag{8}$$

which states the resistivity of a rock (ρ_o) is dependent upon the porosity (φ), brine saturation (S_w) and fluid resistivity (ρ_w). The minor components are the tortuousity (a), cementations factor (m) and saturation component(n). This is not always the case, when the host rock is itself conductive, clays are an example. A common adjustment to Archie's equation, Equation (8) is to add a non-linear shale factor, commonly dependent upon the cation exchange complexes of clays (Waxman et al., 2003).

Distortion of the Electrical Field

Electromagnetic signal distortions are created by geological anisotropies of distinctly separate resistive properties to that of the bulk-resistivity measurement (Marti et al., 2009). Decomposition and distinction between the two major physical processes, galvanic and inductive, help analyse a distorted signal (Groom & Bailey, 1989). Commonplace is to disregard the effects of inductive distortions, due to the relatively minimal variations of magnetic induction held within the Earth (Jiracek, 1990). Galvanic distortions are caused by polar-charged geological discontinuities that produce a localised secondary electrical field ($\vec{E_s}$),

$$\vec{E}(\omega) = \vec{E_r}(\omega) + \vec{E_s}(\omega) \tag{9}$$

that is superimposed upon the regional electrical field response ($\vec{E_r}$). Linearising this creates a proportional distortion vector D_{ij},

$$\vec{E}(\omega) = \begin{bmatrix} d_{xx} & d_{xy} \\ d_{yx} & d_{yy} \end{bmatrix} \vec{E_r}(\omega) \tag{10}$$

decompostion of this vector analyses the three-dimensional twist and shear tensor effects of the observed potential field. Analysis of the tensional variant magnitudes and angles, helps classify the distortion's geoelectric strike orientation and dimensionality (Berdichevsky & Dmitriev, 1976; Jiracek, 1990). An electrically anisotropic Earth can be caused by a multitude of geological phenomena from microscopic crystal morphologies, fluid composition and porosity to the macroscopic accumulations of the same phenomena to which individual features cannot be resolved but are represented in regional estimates. (Marti, 2014).

Phase Tensor

An extension of the impedance tensor first brought forward by Caldwell et al. (2004) represented a new dimensionality analysis technique independent of localised galvanic distortions. Physically the phase tensor represents how adjacent mediums alter the wavelengths (energy) of the incident electric and magnetic waves, relative to regional three-dimensional distortions (Chave & Jones, 2012). The phase-tensor is described as the phase-angle relationship between the real and quadrature (imaginary) components of each MT mode/transfer, Equation (11) (Bibby et al., 2005), formulating a second rank tensor,

$$\vec{\Phi}(\omega) = \begin{bmatrix} \vec{\Phi_{xx}}(\omega) & \vec{\Phi_{xy}}(\omega) \\ \vec{\Phi_{yx}}(\omega) & \vec{\Phi_{yy}}(\omega) \end{bmatrix} \tag{11}$$

capable of resolving regional anisotropy of galvanic distortions in three dimensions with no prior knowledge (Caldwell et al., 2004; Bibby et al., 2005). The tensor components are dependent upon four singular value (de)composites, the coordinate invariants of the major axes of geoelectric variation Φ_{min}, Φ_{max}, α and β are interpreted from Equation (11); the trace, skew and determinant tensor properties (Caldwell et al., 2004).

$$\vec{\Phi}(\omega) = \begin{bmatrix} \vec{\Phi_{max}}(\omega) & 0 \\ 0 & \vec{\Phi_{min}}(\omega) \end{bmatrix} \tag{12}$$

Beta is drawn similarly to Swift's skew, (Swift Jr, 1967) and describes the symmetry of the impedance tensor (Bibby et al., 2005). This is seen as the angle of trace and anti-trace ratios,

$$\beta = \frac{1}{2}\tan^{-1}\left[\frac{\Phi_{xy} - \Phi_{yx}}{\Phi_{xx} + \Phi_{yy}}\right] \tag{13}$$

of the major vector components. A stray from the major axis of orientation ($\beta > 0$) suggests a conductive distribution is present away from Φ_{min} and Φ_{max} axes and is represented by an ellipse. Singular value decomposition of α requires arbitrary rotation of the signal to define the tensor components dependency on the coordinate system. β rotation from Φ_{min} and Φ_{max} axes,

$$\alpha = \frac{1}{2}\tan^{-1}\left[\frac{\Phi_{xy} + \Phi_{yx}}{\Phi_{xx} - \Phi_{yy}}\right] \tag{14}$$

represents the angle between from unit circle origin. The four invariants are used to graphically represent the electrical distortion distributions as an ellipse (Booker, 2014). The value attained, $\alpha - \beta$, represents the elliptical elongation (or inductive distribution) running parallel to the regional geoelectric strike at given frequencies (Simpson &

Bahr, 2005).

Dimensionality analysis of phase tensor decompositions have been extensively described (Caldwell et al., 2004; Bibby et al., 2005; Booker, 2014). There are two-major components to take note of for analysis, the ellipticity β and the induction polarity $\alpha - \beta$. In one-dimension a radius-circle is conveyed, with no deviation in β, however deviations in polarity from 45 degrees represent the 1D distortion effects. In two-dimensions, ellipticity is non-circular suggesting that there is a non-uniform distribution of induction. In three-dimensions and for one-dimensional anisotropic conductive phases the initial explanation in 2D holds, however (β) is non-zero.

A phase tensor misfit can be ascertained,

$$\Delta = \vec{\Phi}_{prior} - \vec{\Phi}_{post} \tag{15}$$

based upon the difference between pre and post-injection phase tensor results Equation (15) (Peacock et al., 2013). This was originally applied for misfit guidance between predicted and observed data, to determine dimensional distortion disparities (Heise et al., 2008; Booker, 2014). By tweaking this technique to monitor the changes occurring temporally, the effective residual tensor plots attempt to show the imposed distortion effects associated with hydraulic fracturing between two time-series windows (Peacock et al., 2013).

MAGNETOTELLURIC DATA

Data Acquisition

Moomba hydraulic fracturing was monitored using 40 quadrupole electrode logging (QEL) to record MT responses for a 65-day recording window: day 137 UTC (17/05), 2014 until day 202 (23/07), 2014. The stations were set in a cross-array at 200 m separation, Figure 1 and Figure 3. A magnetic remote reference station was also established 3 km SW of the major array, to enhance signal recovery, particularly useful in reducing dead-band noise (Gamble et al., 1979). Directional drilling lay within the southern quadrant of the station array Figure2. QEL stations measured the orthonormal components of the electrical field ($\vec{E_x}$, $\vec{E_y}$, $\vec{E_{x'}}$, $\vec{E_{y'}}$) and two magnetic field components ($\vec{B_x}$, $\vec{B_y}$), Figure 3. This allows for dipole preferential processing and typically increases the likelihood of improved signal coherency (Gamble et al., 1979).

Each station utilised a 16 m quadrupole electrode complex for potential difference measurements in time, Equation (1), recorded by solar-powered e-loggers, Figure 3. Station e-logger PR6-24 Portable Field Recorder, sampled 21-bit potential difference data at 651 Hz for all four channels. PMS 9000 electrodes using $Pb - PbCl_2$ electrolytes for durable salt diffusion, essential for 65-day monitoring schedule. LEMI-120 magnetic induction coils sampled the magnetic field strength ($\vec{H}$) at 651 Hz for effective 21-bit data as well.

Data Processing and Quality

Time-series plots provided initial insight into station data quality, identification of station dipole preference (quadrupole benefit) and the time-duration of instrument recording from Figure 4 and Appendix 1. Input of station time-series to Bounded Influence, Remote Reference Processing, BIRRP (Chave & Thomson, 2004), produced estimates of

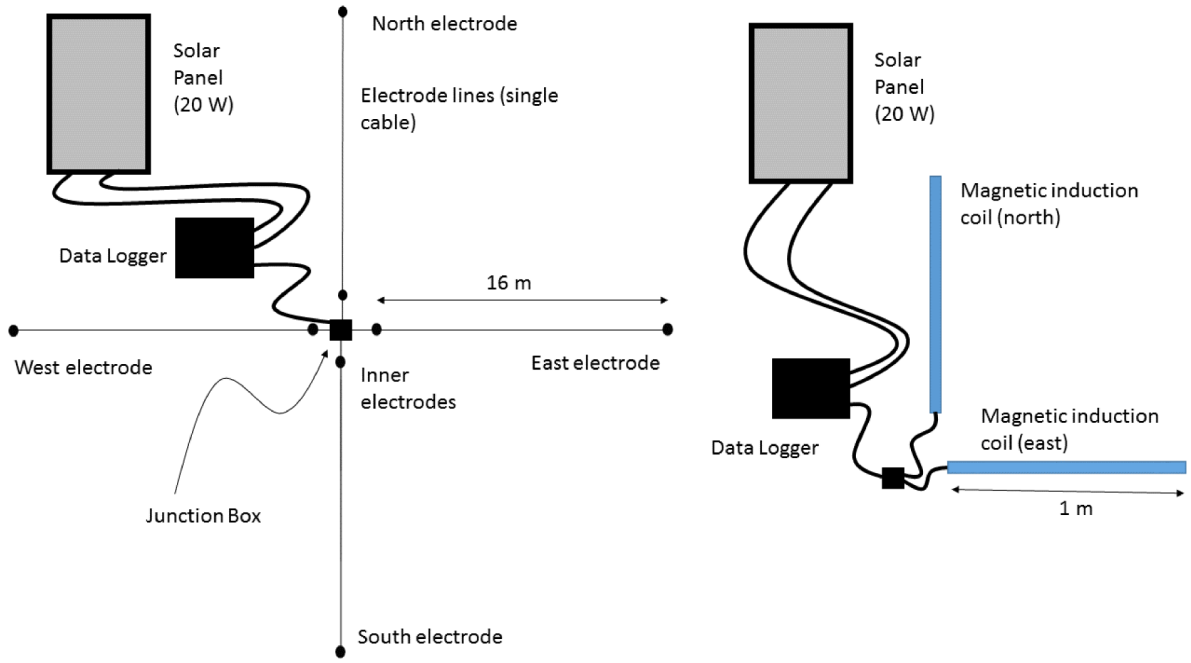

Figure 3: Diagram of a typical quadrupole electrode magnetotelluric station. The figure shows the inherent difference to conventional MT stations set-up as there are an extra set of measurements of the south and western propagating fields. Individual electrode dipole lengths were set for 16 m. Solar-panels were used to ensure logger power throughout surveying. The induction coils do not require an extra-set as geomagnetic variations are minute in comparison.

the impedance tensor components, plotted in Figure 5. The BIRRP process decimated the data to 500 Hz, to band-section average prolate Slepian window functions from 12-hour daily windows at 20 million samples. Low-pass filtering attempted to attenuate the effects of high-frequency data, and notch-filtering reduced the effects of long-wavelength inductions. A second notch-filter was used to reduce noisey signal at 0.25 Hz.

Remote reference data are normalized to reduce the effect of localised magnetic signal distortion,

$$Z = \frac{E \cdot B_r^H}{B \cdot B_r^H} \tag{16}$$

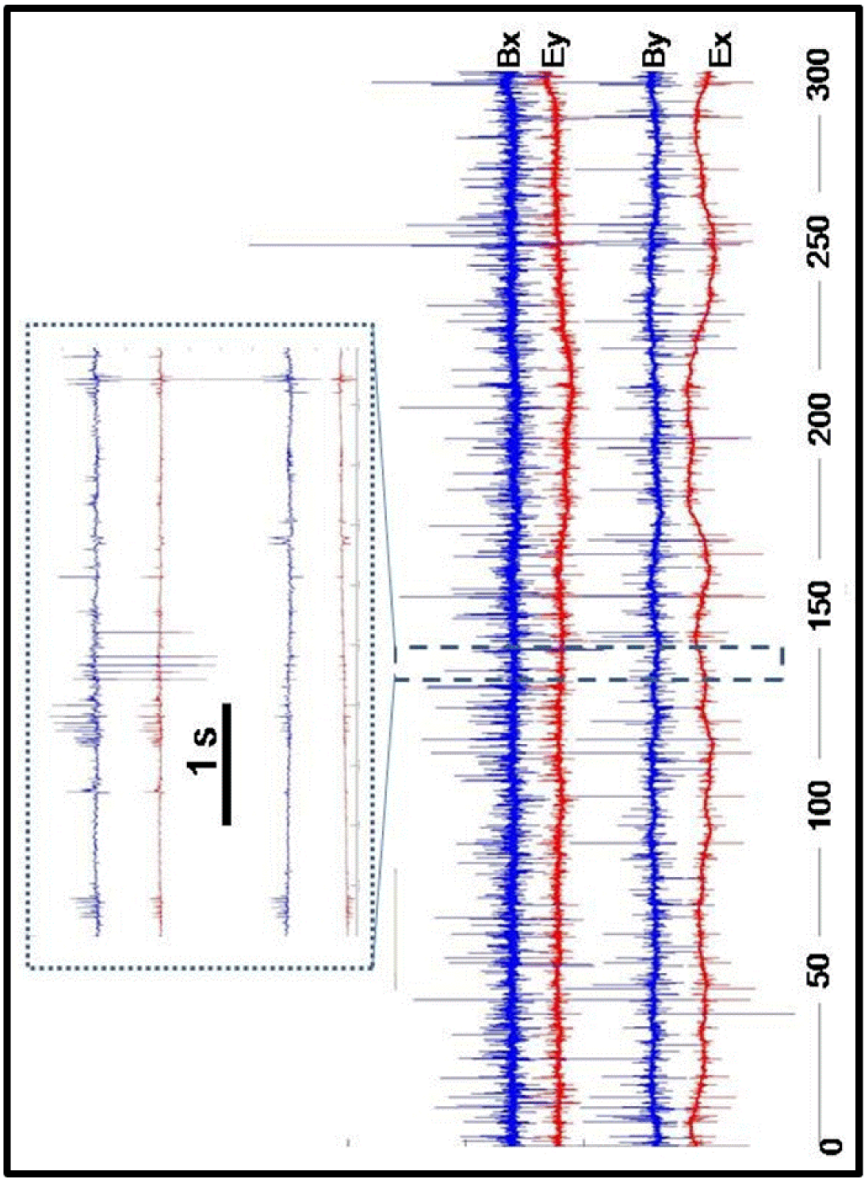

Figure 4: Time-series measurements of the electric and magnetic field from south-west components. Data shown are from station 22, day 142 UTC. The bottom time-series show the long period correlation (300 s) between electrical field components and the top time-series shows the same for 5 seconds. The series are aligned for visual identification of component correlation (4).

Hermitian (exponential H) transpose vector correlation assesses the differences between the locations (Chave & Thomson, 2004). Through jack-knife estimations of tapered M-estimated windows, BIRRP robustly computes apparent resistivity and phase averages with standard errors for each component (Chave & Thomson, 2003; Chave et al., 1987).

The time-series were analysed between the bandwidth 0.01 Hz and 100 Hz, for 10 estimations per decade period. Large error estimates are still observed in the dead-band frequencies 0.5 Hz - 5 Hz, however windowed- estimates outside of show high-quality estimates spanning less than 3 % of ρ_a. Periods within than the dead-band are vary greatly, typically they are greater than 20 % (up to 200 %). The error estimates are less pronounced in $\vec{Z_{yx}}$ than $\vec{Z_{xy}}$. Phase estimates outside the band are all within 1 degree, however within some are as high as 20 degrees.

RESULTS

Dimensionality

Analysis of the dimensionality, deduced from impedance tensor decomposition using WALDIM codes (Marti et al., 2009) and phase tensor analysis have shown sensitivity to the induced distortion (Caldwell et al., 2004). WALDIM analyses seven separate sets of independent invariants (and a dependent invariant) of the impedance tensor to decipher the induction dimensionality. Impedance tensor decomposition is then categorised into the distortion type and dimensions through factorisation of the invariants. The invariants l_7 and Q are compared to determine distortion type and three-dimensionality (Marti et al., 2009). Currently the invariant error bars are less than 10 % of the value for l_{3-6} suggesting two-dimensional interpretations hold sufficient interpretation. However

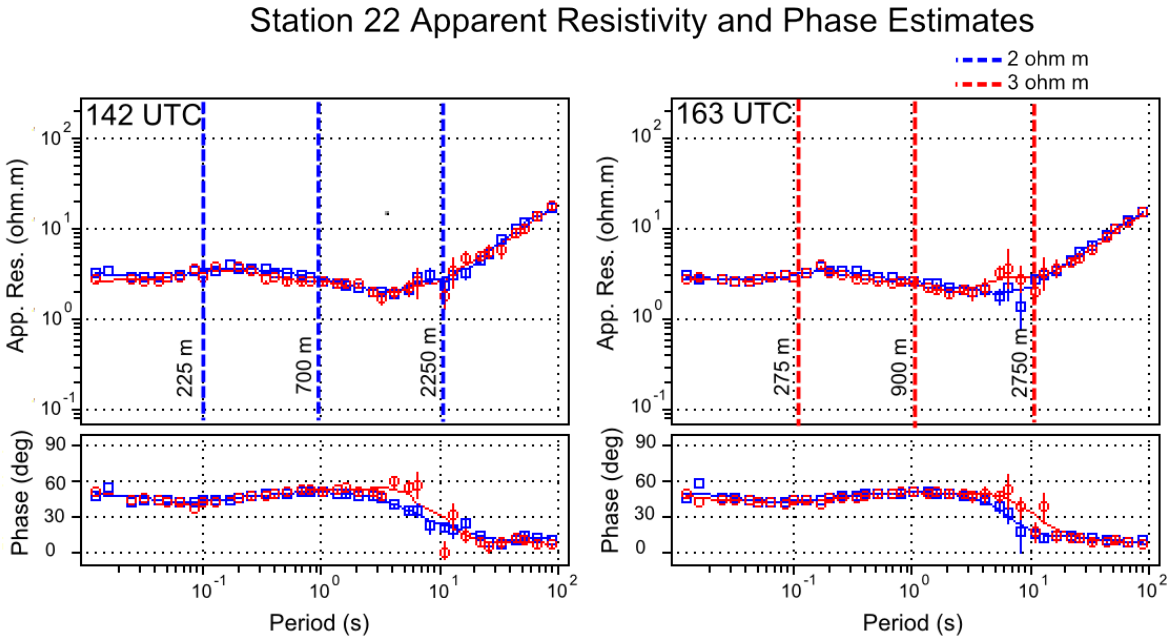

Figure 5: Two-date apparent resistivity and phase plots. These charts attempt to show the differences in site impedance estimates from 142 UTC and 161 UTC. Manual masking of data-frequencies with large error-estimates reduced model RMS values and enforced model through two standard deviations estimates. Applying simple skin depth calculations to the average resistivity values at each decade provides for depth correlations, the dashed red lines show the calculated depths at periods for bulk resistivity estimates of 2 and 3 Ωm.

l_7 and Q hold errorbars typically greater than 100 % of the mean value, suggesting poor decomposition quality and imposed three-dimensional regions (Groom & Bailey, 1989).

The outputs from WALDIM and the interpreted phase tensor, Figure 6 and Figure 7, should adhere to similar distortion dimensions. At low frequencies static-shifting is apparent from this discrepancy (Marti, 2014). Dimensionality between the two are distinctly different at low frequency bandwidths, the WALDIM estimates show two dimensions and the phase tensors suggest one dimension. At similar periods (roughly 6 seconds), both models take three-dimensional characteristics - however this is likely not coincidental due to increased error estimates from external noises in dead-band frequencies. Rotation of the data typically amplifies the error estimates of the impedance and

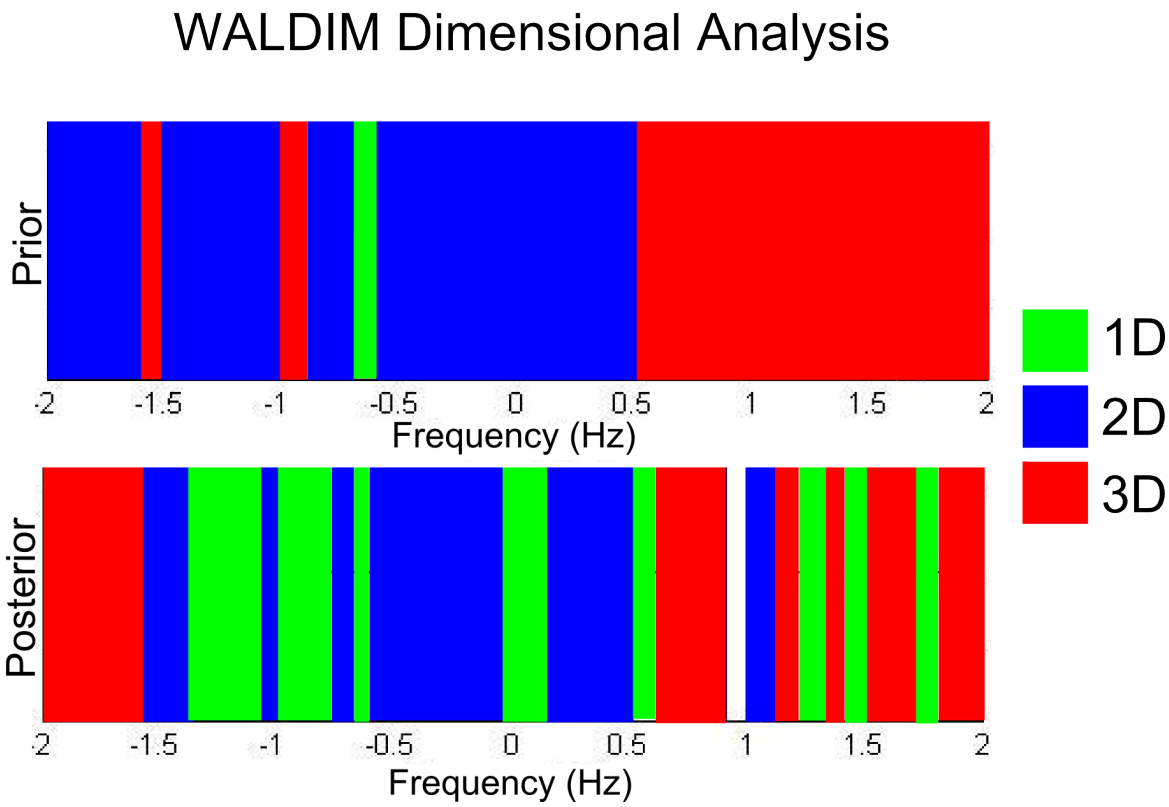

Figure 6: An algorithm to analyse the 8 sets of rotational invariants from WAL criterion. The threshold limit of data errors was set to 10%. Two invariants are dimensionless and used to normalise the other components (l_1 and l_2), from 1D magnitude and phase elements (Weaver et al., 2000). Four components (l_3, l_4, l_5 and l_6) are analogous to the phase tensor and the output should adhere to the same dimensions as the tensor ellipses (Weaver et al., 2006). High errors have caused high invariant error estimates, particularly notable in invariant l_7 which assesses whether a structure is 3D (Marti et al., 2009).

phase tensors (Jones & Groom, 1993)

Layers A-C reference the dimensionality of distortion in their respective bandwidths, to which A is 2d, B is 1D and C 3D. The phase tensors of periods > 10 seconds in line 2 show the only induced trend, phase-tensor orientations greater than Caldwell (2004) mean cut-off induced (3^o), to which the angle of geoelectric strike orientation east, Figure 7.

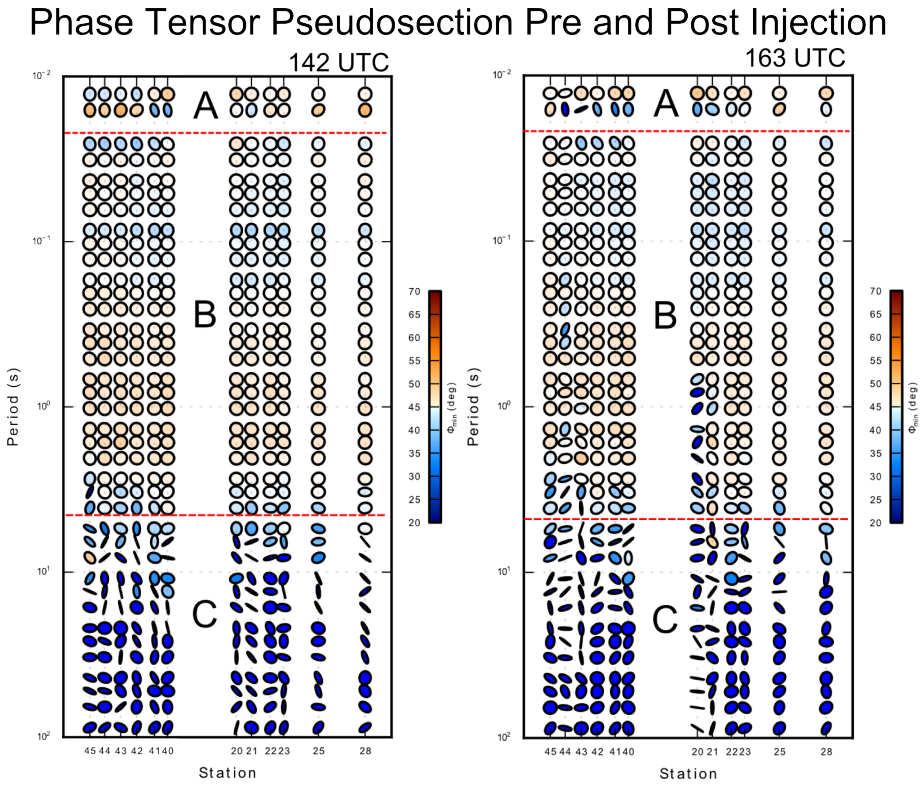

Figure 7: Pre and Post-injection pseudosections of the phase-tensor ellipses. The pseudosection shows stations with sufficient data quality, attempting to show induction gradient changes experienced from injection. The measure of Φ_{min} in degrees shows the axis orientation of geoelectric strike in two-dimensions. The separate layers labelled alphabetically represent tensor bandwidths of differing distortions. The layers are interpreted from the skew values: A holds 1D distortions and B, 3D These were produced following Caldwell (2004) and Bibby et al. (2005) and implemented using MTpy (Krieger & Peacock, 2014).

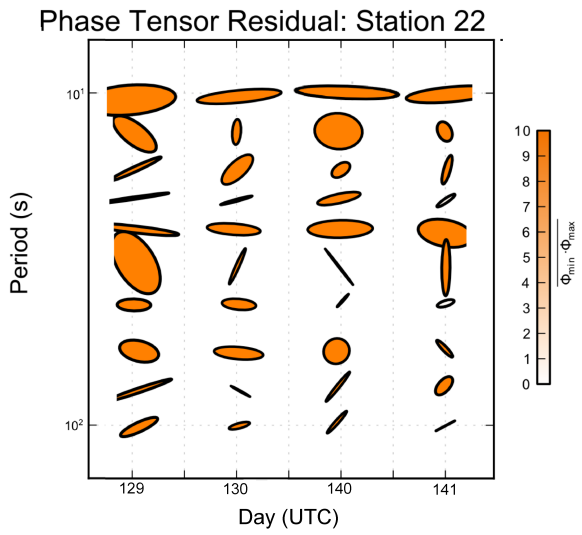

Figure 8: Residual tensor measuring the phase-tensor ellipse differences between day 142 UTC (22/05) and the highest quality days represented on the date axis. The higher frequencies have been omitted as they show negligible changes between dates. There is a trend of horizontally constrained ellipses, the effect appears to be localized only affect periods greater than 10^o. The periods below these show negligible effects. These have been calculated based on Equation (15), (Booker, 2014; Krieger & Peacock, 2014).

RESIDUAL PHASE-TENSOR COMPARISON: PRIOR-POST

Phase tensor residuals, Equation (15), were calculated to show the alterations of galvanic distortions from hydraulic fracturing (Peacock et al., 2013). Figure 8 shows the galvanically distorted changes from day 142 UTC to the day referenced on the x-axis. Frequencies higher than 0.1 Hz yielded negligible changes in distortion ($\sqrt{\Phi_{min}\Phi_{min}}$ ¡ 0.2) between each date and so have been omitted, however for frequencies shown differences greater than those expected from the noise show a directional trend. The horizontal trend is indicative of a distortion of geoelectric strike east of station 22. Currently the phase-tensor suggest three-dimensions are required for sufficient inversion representation, this will be reviewed upon new impedance estimates.

Inverse Modelling

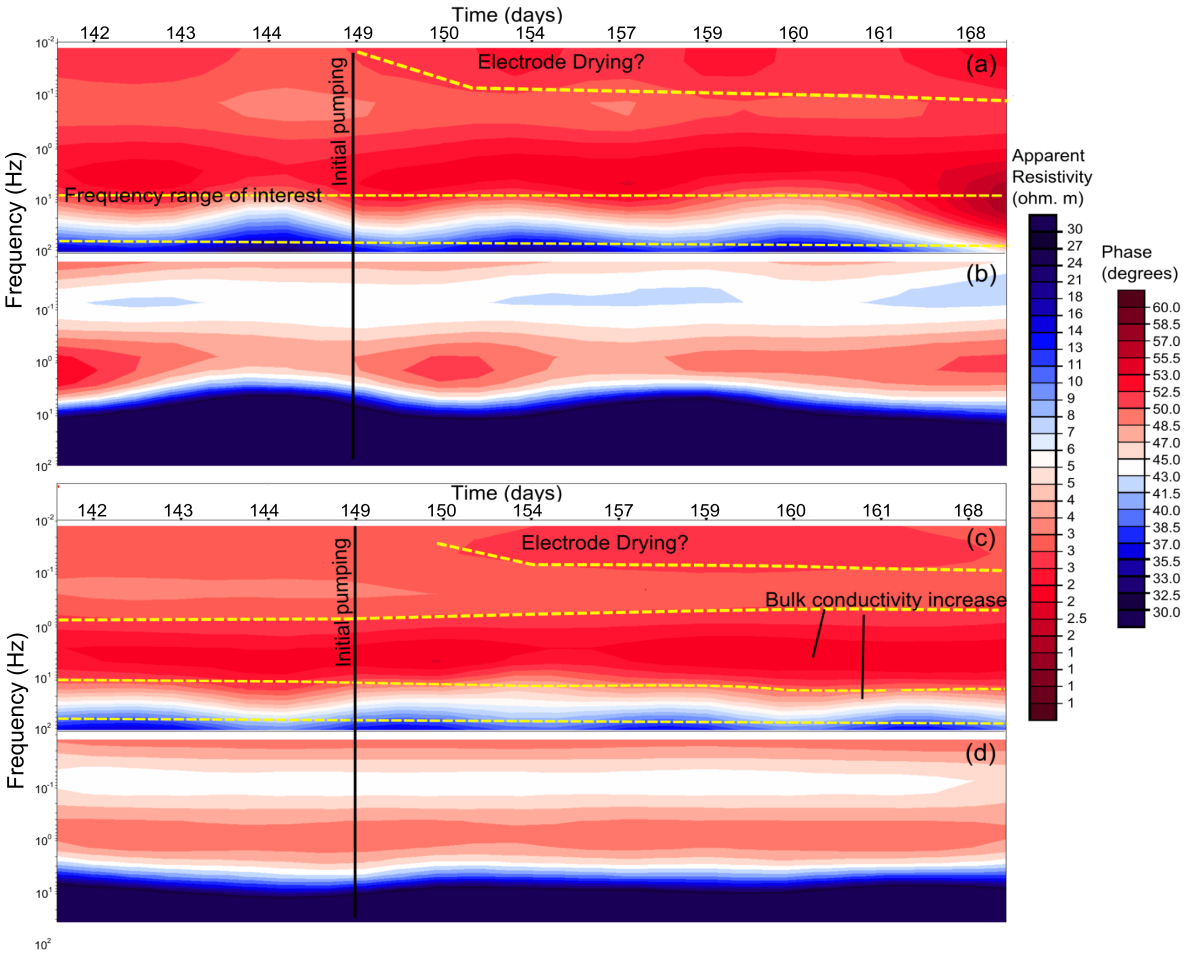

Figure 9: A pseudosection of station 22 through time. The x-axis is a pseudo-time representation with one day represented as 200 m. The spline interpolation between the sites was defined by a step-function (0.2 km) by a 7th order spline for smoothness. The interpreted lines show the conductive increase at depth, potentially recognising bulk resistivity changes. The stations used are of the higher quality day-sets. a)resistivity TE b) phase TE c) resistivity TM d) phase TM. Created in WINGLINK.

1D MODELLING

WingLink implements an algorithm following Occam's inverse solution for interpretation of resistivity and phase in one-dimension (Constable et al., 1987). Occam's inversion forward models the electromagnetic wave equation to find the smoothest model that fits

the data, an RMS of 1.5 is generally considered ideal, a compromise of overfitting and underfitting the data. The basis models were set from an initial resistivity of 3 Ω m and an *a priori* 5-layered Niblett-Bostick model for a depth range between 70 m and 12,000 m. Gridded element modelling subdivides the inverse functional operator into a series of 45-layered resistivities. Occam 1D models were adjusted for static-shifting of TE mode, altering the scalar effects based on the less affected TM mode. Inversions ran for 50 iterations before converging to a maximum percentage RMS of 5%.

Due to the greater precision held at station 22, a pseudo-section of Z_{xy} (TE) and Z_{yx} (TM) align the higher quality daily observations along a profile with a separation of 200 m to represent quasi-time in Figure 9. The difference between the modes show that TM mode recognises a conductive contrast greater than in TE and that there is less variation between TM mode impedances than those seen in TE, a property of reduced susceptibility to static-shifting. At low frequencies in 9.c (0.01 Hz to 1 Hz) a conductive increase is observed and an increase in the wavelength to the basement. An increased depth to basement may correspond to an increased regional bulk resistivity at lower frequencies induced from pumping or static-shifting. Due to the procedure at hand, changes at high-frequencies are not expected, there are many possible explanations to the causes e.g.: instrumental-drift, potential noise from nearby operations and more. Due to the unconventional longevity of this survey, dehydration of electrode contact points might have played a role in observable drift showing similar characteristics to a topographic distortion.

2D MODELLING

Increasing the analyses to two-dimensions utilises an algorithm created to supply modelling mesh nodes (Rodi & Mackie, 2001) whilst following the (deGroot Hedlin & Constable, 1990) structure for resolving resistivity inverse problems. The 2D algorithm is an

extension of the 1D smoothing model, discretising rectangular prisms of constant conductivity to the users definition. Joint inversion of Z_{xy} and Z_{yx} attempted to minimise the RMS subject to penalties in model roughness, to which an τ value of 10 optimised the RMS and roughness outputs (deGroot Hedlin & Constable, 1990). The code also attempts to adjust for static-effects via Groom-Bailey (1988) decomposition, a summation of the both mode static-shift effects equating to zero. A non-linear conjugate gradient (NLCG) solves Tikhonov regularised 2D problems from a quasi-linearised diffusion model (Ogawa, 2002). WingLink uses the NLCG method for effective smooth modelling, to find local RMS minima searching via step-function conjugate gradient coefficients γ and ψ (Ogawa, 2002).

Basis models of a 7 Ω m upper half-space and 32 Ω m lower half-space (3600m) were used for minimal biasing. Input of stratigraphic interpreted boundaries into new basis models did not provide any additional information than the 2-layer basis model. Increased node density was placed near the surface (for static-distortion resolution) and between 2600 m and 3400 m (for expected induced anomaly). The inverse algorithm ran for frequencies between 0.01 Hz and 100 Hz, at an attempted 500 iterations, however all converged to the minima RMS before this seed. For basin modelling, γ (1) and ψ (1) were chosen to be small for no horizontal or vertical step scaling to identify smaller-scale anisotropic anomalies. The model roughness penalty was set at an optimal τ of 10, after multiple trials to find a compromise of minimizing roughness (χ) and normalised RMS values. Estimate error floor margins were set to 10 % and 5% for resistivity and phase respectively.

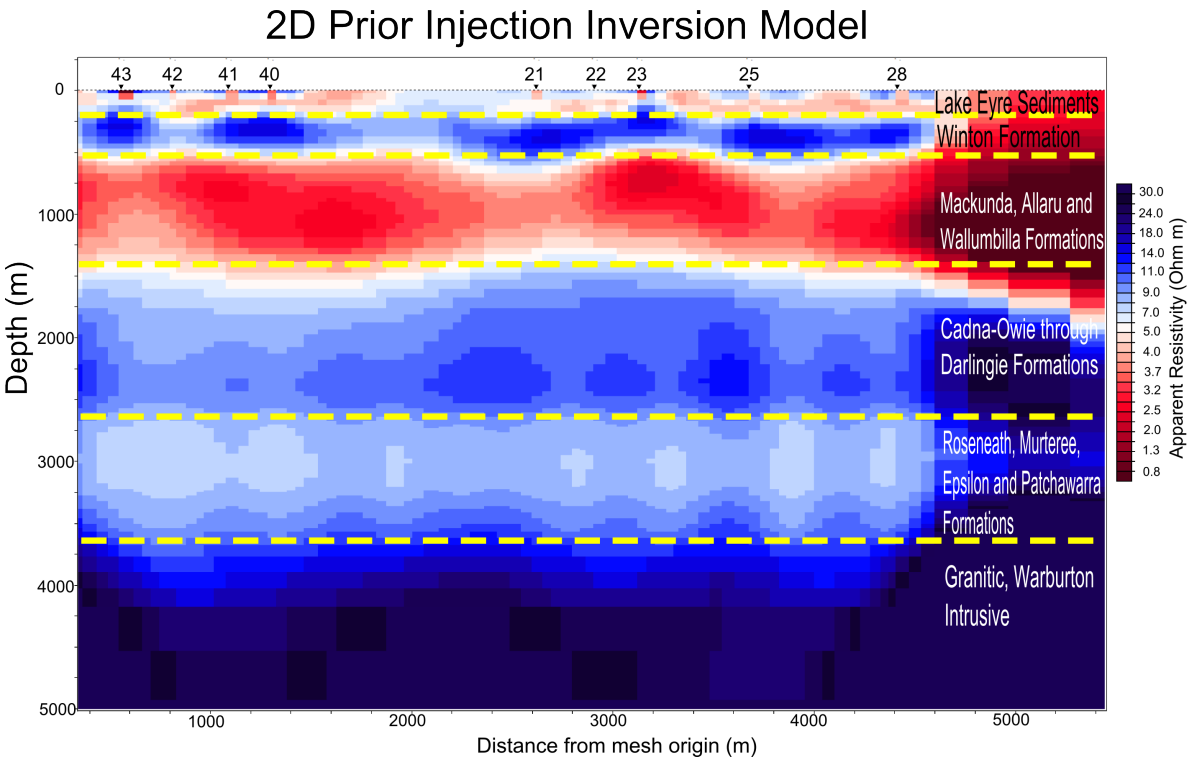

Figure 10: Occam's 2D inversion of the post-pump profile (Day 142 UTC). Inversion of TM mode at a τ of 10 converging after 173 iterations, with a final normalised RMS value of 1.9 and roughness of 315. Inversion was from a basis model of 2-layers, A 7 Ωm top-layer and 37 Ωm bottom layer at 3600 m. Joint inversion provides for a more precise depth-model due to static-shift corrections. Through time the conductive formation expands and grows more conductive. Inversion from Winglink.

The pre-pump inversion ran for 173 iterations converging at a final RMS of 1.9 and a χ of 290 in Figure 10. The model shows eight distinct layers of resistivity, with the range of resistivities between 1-100 Ω m. There is a distinct difference between the two lines to which line 4 shows a larger homogeneous conductive body within the range of predicted shale-fracking (3000 m). Line 2 on the other hand shows anisotropic horizontal layers.

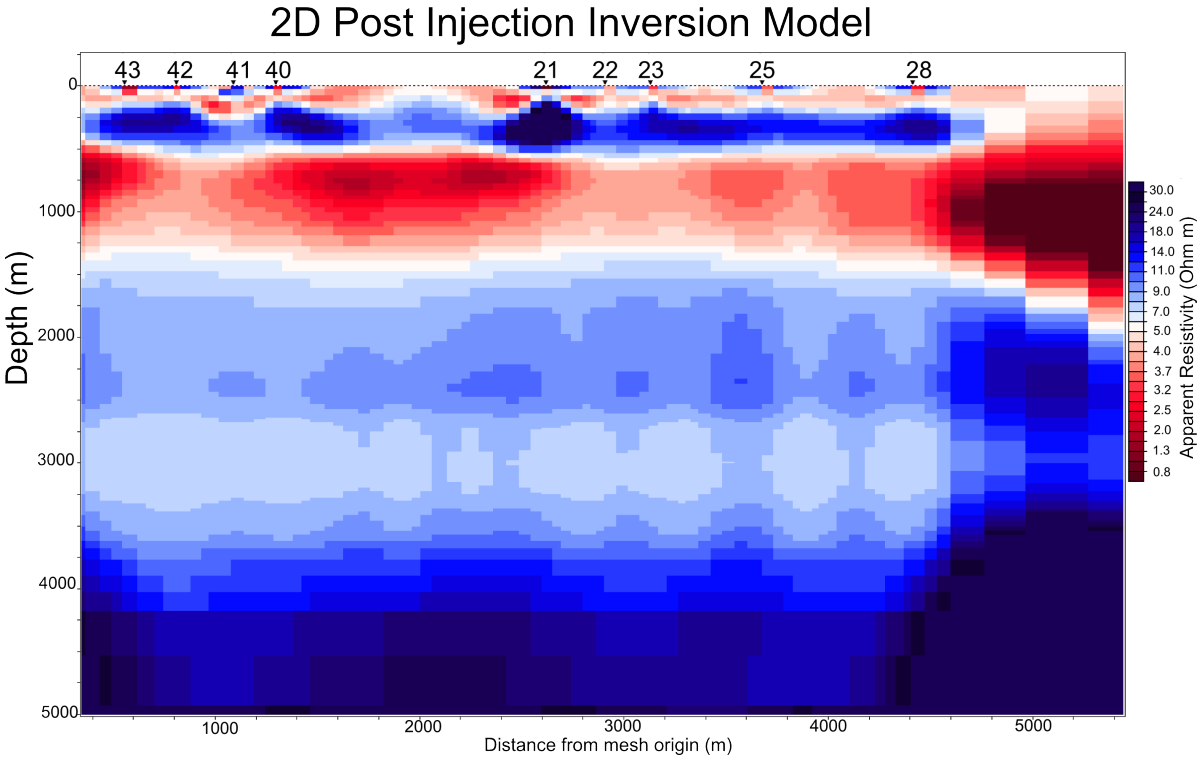

Figure 11: Occam's 2D inversion of the post-pump profile (Day 161 UTC). Inversion of TM mode at a τ of 10 converging after 138 iterations, with a final normalised RMS value of 2.3 and roughness of 315. Inversion was from a basis model of 2-layers, A 7 Ωm top-layer and 37 Ωm bottom layer at 3600 m. Joint inversion provides for a more precise depth-model due to static-shift corrections. Through time the conductive formation expands and grows more conductive. Inversion from Winglink.

The post-pump inversion ran for 138 iterations converging to a final RMS of 2.3 and a χ of 315, Figure 11. The same resistivity discontinuities are present at similar depths to the prior inversion, however alterations of layer-resistivity can be seen from depths greater than 1600 m - comparing Figure 10 and Figure 11. The post pump stage typically shows reduced resistivity within the layers, suggesting the bulk-resistivity estimates have increased or static-shifting has 12. The large variations in resistive change overlying the projected shale injection portray the large apparent resistivity error estimates. The residual cross-section also shows the minor changes, yellow bands of 1 Ω m exhibited within the shale itself.

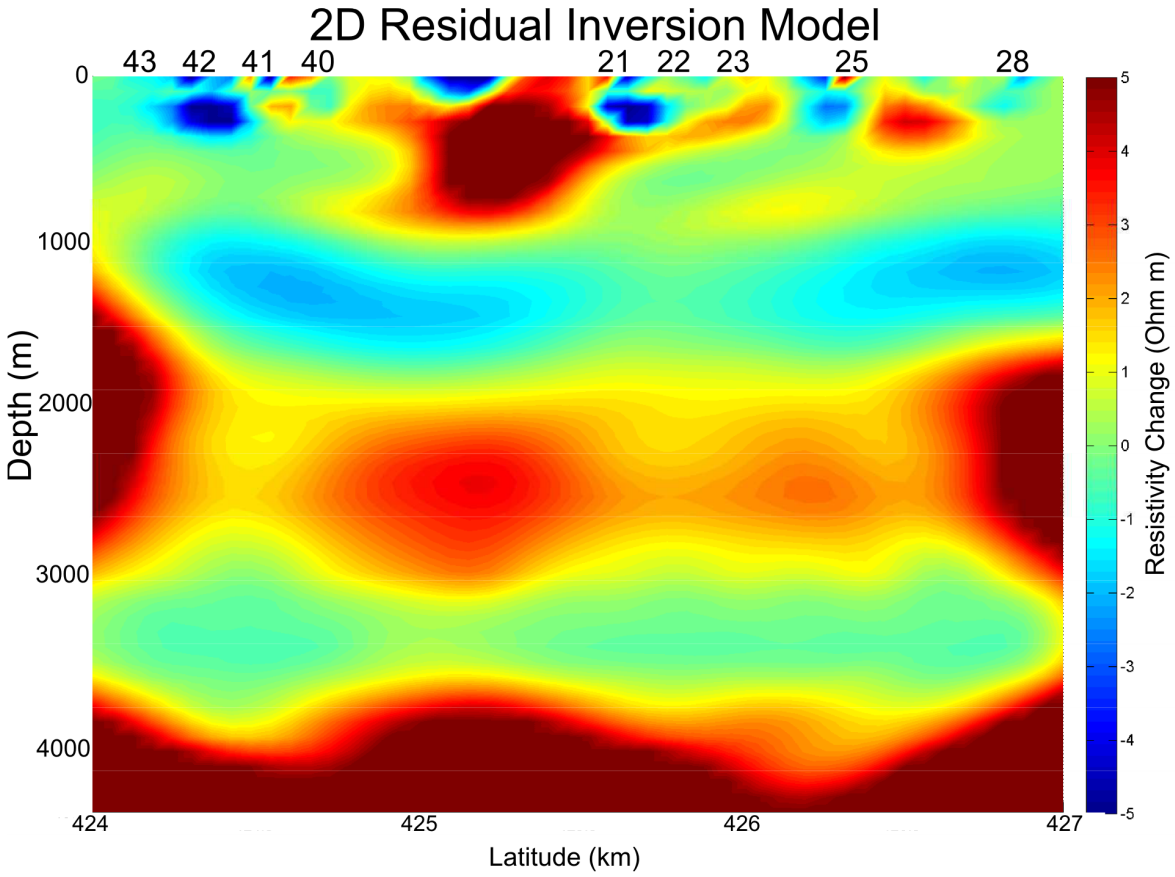

Figure 12: Spatial residual of inverse models: pre and post injection. This is simply the difference in resistivity values of each spatial mesh node. Increases in conductivity are shown as positive values and reductions negative. Between the dates, currently, the largest changes are held within the depth range directly above expected inclusion changes. These show an increased conductivity after the final phase of pumping. The inconsistent residual map, is more likely showing nothing more than that the data is highly variable.

COMPARISON OF POST-INJECTION MODEL

Mapping the changes from the injection was attempted using multiple basis models, blank canvas, pre-inverse and post-inverse basis models to name a few. The attempts to recover base-changes were mostly ineffective, with inversion of lone TM inversion depicting the greatest changes in spatial inversions. The greatest variations between the models appear in the depth range directly above proposed injection and also directly below. A consistent increase in conductivity is observed, and further highlighted from the residual map in Figure 12. Within the shale-layer, the minimum resistivity is 12 Ω m and appears more laterally uniform with greater regional influence.

Station 22 has shown the best error estimations of mean resistivity and phase values. The inversion model was set-up similarly to the 1D pseudosection, Figure 13. The control days show similar characteristics to resistivity vertices in profile modelling however the extent of change is greater. Sampled days used in the inversion show minimal changes after the first two days of pumping (149 and 150 UTC). An influx of pore fluid increased the distortion to which day 154 UTC shows the first sign of sensitivity to induced content. Station 22 shows a body of increased conductive phases from fracturing, spreading predominantly vertically and increasing the regional vertical spread by 2 Ω m. Further improvement of the data to this site and other sites for every day, could allow for a similar day-by-day inversion however for all stations in the profile. If this effect is not unique in its conductive growth, then day-by-day profiling may provide effective spatial domain interpretation of conductive growth through time.

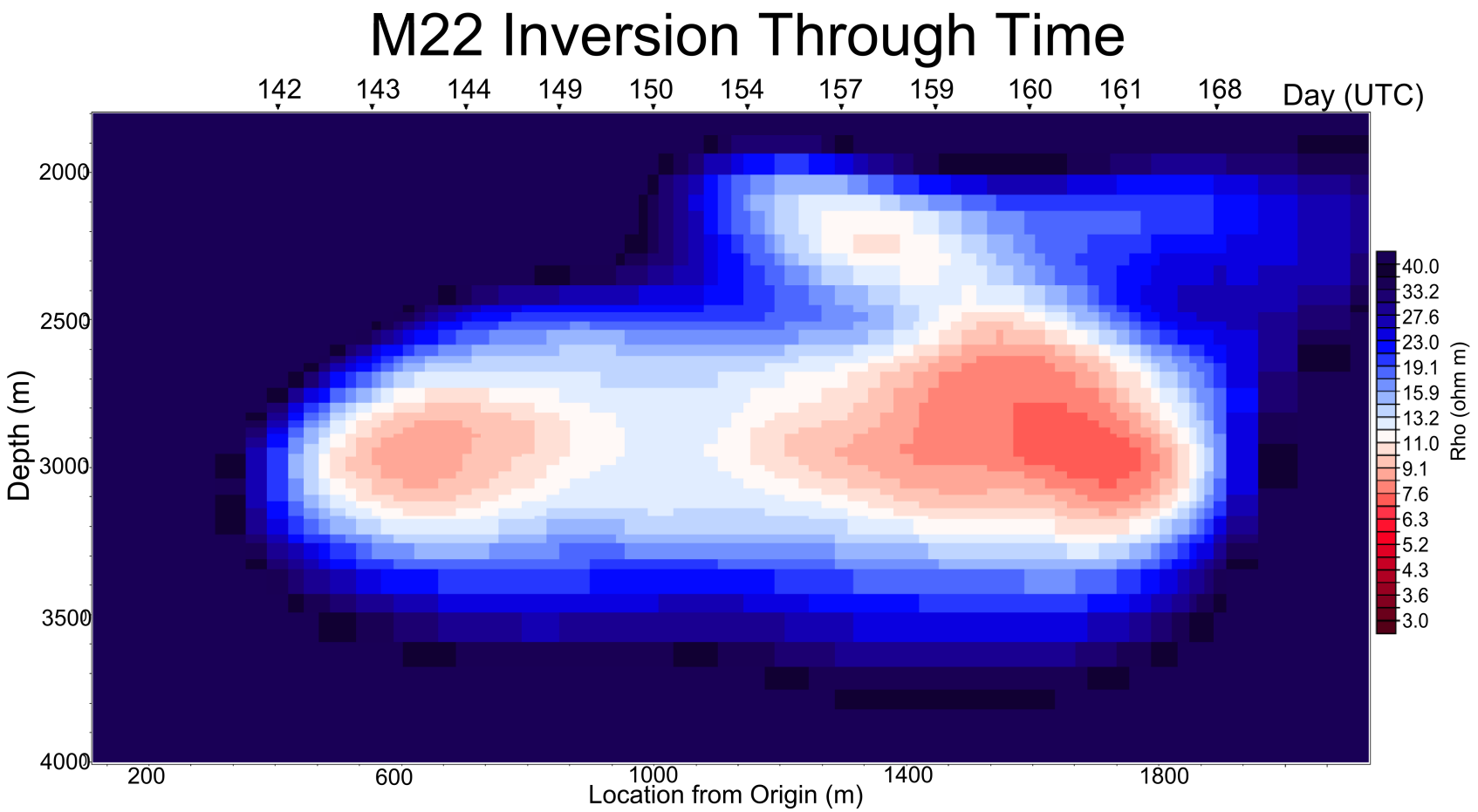

Figure 13: Occam's 2D inversion of station 22 through time. Joint inversion of TE and TM mode at a τ of 1 converging after 373 iterations, with a normalised RMS value of 2.1 and roughness (χ) of 280. Inversion was from a basis model of 2-layers, A 7 Ωm top-layer and 37 Ωm bottom layer at 3600 m. Joint inversion provides for a more precise depth-model due to static-shift corrections. Through time the conductive formation expands and grows more conductive. Inversion from Winglink.

DISCUSSION

Inverse Modelling - Basin Interpretation

The eight-layer resistivity interpretation in Figure 10 has been classified by sequence apparent resistivity values and lithological studies within the Cooper Basin (Apak, 1994; Alexander et al., 1996; Ahmad, 2014). The basin shows horizontal bedding through till depth. The conductive Lake-Eyre sediments represent the top 200 m of the cross-section, reading low resistivity (7 Ω m) inferring saline surface water content and high porosity. The shallow regions of the Winton Formation are relatively resistive at 27 Ω m, indicative of a low salinity aquifer within the formation (Palacky & West, 1991; Fulton, 2012).

The Mackunda Formation bears low saline water content however the base of the formation has been shown to hold a pyritic matrix (Fulton, 2012; Alexander et al., 1996). Pyritic dissolution could create for the dissemination of sulphides, known for their semiconductance and high conductivity (Nabighian, 1988). Overlying formations are highly concentrated in clay laminations. Clays typically express high cation exchange complexes (CEC) transmitting a signal of high conductivity in the presence of even slightly conductive electrolytes (Nabighian, 1988; Alexander et al., 1996). The claystone laminants present in the Mackunda, Allaru and Wallumbilla formations produce a near continuous layer of 2 Ω m at 800 m - 1600 m. The denoted Cadna-Owie layer in Figure 2 is interpreted as a congregation of similar resistivity characteristics. The earliest Eromanga Basin sediments hold multiple major aquifers that are extensive throughout the depth range 1600 m - 2400 m. All are relatively pure, laboratory salinity estimates are below 6000 μS, ten times less than sea-water (Fulton, 2012). The Cooper Basin sediments overlying Roseneath deposition are sandstones of elevated hydrocarbon content (Alexander et al., 1996). Two distinctly separate facies have been interpreted as a

relatively resistivity medium from 16 Ωm to 32 Ω m between 1600 - 2700 m.

The zone of interest (Roseneath) bears low resistivity, this predominantly shale-region holds high clay (predominantly kaolinite and illite)concentration at 55% (Phillip, 2013). Clay boundaries exhibit concentrated CEC and the water within tends to hold high total dissolved solids, generally creating a highly conductive anomaly (Waxman et al., 2003). The inverse model suggests that the shale is anisotropic in its conductive phases, to where the sites proximal to pumping (line 2) show non-uniform lateral magnitudes.

Basement granite rocks from the Warburton Basin are marked as the highly resistive structure present as the last transition of the frame. Crystalline rocks due to low permeability and composition tend to resist electrical flow at these prescribed temperature and depth conditions (Nesbitt, 1993).

Factors Affecting Resistivity

The introduction of ionised fluids into an artificially induced permeable pathway, should permit for high electrolytic conductance and thus increasing the bulk-conductivity of transmitted waves (**?**; Waxman et al., 2003). The conductivity of formation fluid is proportional to the fluid composition, saturation, porosity and temperature conditions within the rock (Nesbitt, 1993; lan Gough, 1986). Introduced fluids to the geotherm (40^o C km^{-1}) approximate to an inclusion fluid temperature of 120° (Beardsmore, 2004). Empirical studies suggest that a saline body (10-24 w%) at these temperatures, with Archie's equation s fluid resistivity estimate of the order 10^{-2} - $10^0\Omega$ m provided effective porosity permits fluid flow (Nesbitt, 1993). With a suspected increase in intergranular porosity, it is likely that this should further increase the conductive anomaly present (Archie, 1942). Kaolinite clasts encompass over 50% of the Roseneath Shale's material, suggesting con-

ventional Archie's Law approaches will likely mislead interpretation as host clay CEC typically increase the electrical conductance (Waxman et al., 2003; Weaver, 1989). Without the provision of access to fluid inclusion properties and induced permeability records, estimations of Archie's Law (1942) are speculative at best. Due to the permeability, temperature, volume and total dissolved solids of clay content the induced anomaly is expected to have a significant decrease in fluid resistivity, however due to the large volumetric measurement of overlying bulk-resistivity the effect is likely to be reduced (Marti et al., 2009). Hydraulic fracturing typically creates dense pockets of effective porosity in regions of mechanical failure. Typically the principle stresses at depths greater than 1800 m provide for greatest strain from overburden pressures resulting in vertical fracturing (**?**). Extreme pressures can cause the relatively unstable shale to fail in multiple directions representative of horizontal principle stresses (**?**). Vertical fracturing is suggested from the increased vertical growth of conductivity.

Induced Distortion from Hydraulic Fracturing

Impedance and phase-tensor analysis do not provide for convincing interpretation at present. Trends within the phase-tensors of higher quality estimates (station 22) show a potentially induced two-dimensional resistivity structure within a bandwidth analogous to those predicted from skin-depth and apparent resistivity estimates,Figure 9 and Figure 5. The trend through time, suggests that with increasing introduced fluid volume, the ellipticity of the tensor becomes more elongate and further strays from one-dimensionality **??**. The major axes of the phase components are orientated near horizontal, proposing an induced (at least) 2D distortion in the data trending east. Gradual increases in the difference between the phase-tensor residuals, show induced distortion sensitivity to the injected fluid volume. With increased error estimates, it is plausible that spatial phase-tensor inversion can show the direction towards the greatest induced fracture

densities (Heise et al., 2008). Upon well-equilibration, the phase-tensor outputs could be used as a proxy for potential well-locations. Phase-tensor and WALDIM analysis suggest that 3D inverse modelling is required to resolve the distribution effects (Marti et al., 2009; Ogawa, 2002; Siripunvaraporn et al., 2005).

Currently one and two-dimensional modelling of two dates do not portray significant electrical resistivity changes induced from a ten-stage fracking procedure. Changes are shown in separate inverse models, however due to the small increase in resistivity and high error estimates within the region, no conclusive portrayals are revealed. Utilisation of the high-quality estimates of station 22 and imposing multiple dated measurements to a two-dimensional inversion depict a gradual conductive increase through time **??**. The inversion results suggest the effects of the inclusion are localised at 2950 m depth with increased conductivity estimates (1-2 Ωm) spreading through a 300 m vertical zone. Primary vertical fracturing is suggested, with fluid dispersion of 300 m proposed from the increased conductive body. Fracking began at the southern tip proceeding north, with influx of material closer to station 22 later in the procedure, reflected by the right hand side of Figure **??**. Significant changes to higher frequency data are suggested from 1D modelling 9, but not expected due to the frack inclusion or from forward modelling. A static-shifting affect is likely, no phase changes, significantly reducing the ability to accurately map out depths (Ogawa, 2002).

Studies on the effects of an induced anomaly into an EGS (Paralana, South Australia) produced far greater resistivity residuals (Peacock et al., 2012). Peacock et al. (2013) utilised the phase-tensor heavily to analyse regional distortions, this was particularly so due the experienced: expected noise and instrumental shifts throughout a long surveying period. This study has been perceived as less conclusive, leaving the question as

to why this technique was more successful at a location only 100 km away. One major difference between the surveys are the fracture front properties. Paralana's enhanced geothermal system follows elongated regional faults, whereas this study the network is likely fragmented with re-activation of large faults highly unlikely. Fractal resistor network modelling have shown that fragmented regions of localised electrical flow are more resistive than unsegmented induction, similar to that of an elongate fault (**?**). Another potential factor is eluded to in the paper: a potential intersection and mixing fluids of the induced fracture front and from an active fault. The predicted anomaly appears four-times greater in volume than expected (Peacock et al., 2013), greatly enhancing magnetotellurics ability to detect bulk-fluid movement (Chave & Jones, 2012). Lastly the lithology at Paralana holds far less clay content and shale products. Shale effects enact differently under two major conditions: pH and salinity (Wang et al., 2006). Under mildly saline conditions the formations resistivity can exhibit the same inductive effects as under highly saline, therefore whilst there is an influx of ionic material it does not necessarily result to increased resistivity estimates. Clay clast electrical resistivity is highly dependent upon the pH conditions, to where an increase in pH causes an increase in resistivity (Revil et al., 1998). Commonly refined proppant fluids hold high pH values, potentially reducing the effect of clay minerals and balancing the induced effect (Maxwell et al., 2010). Hydrocarbon displacement of formation fluids can also cause an increased resistivity effect, to where pore-space hold greater concentration of resistive molecules (hydrocarbons) (Waxman et al., 2003). The study (Peacock et al., 2013) does not provide inverse solutions, based on the forward models proposed, the injection seems likely to bear a greater resistivity contrast to the host than this case, enhancing magnetotelluric susceptibility.

Improvements

Alteration to the dipole lengths could potentially provide for greater resolution in future surveys. By increasing the dipole length to 50 m or more, the increased electrical field resolution could allow for greater edge-effect resolution (Chave & Jones, 2012). Utilisation of a secondary remote reference magnetic field station could produce greater correlations to identify and remove localised magnetic distortions (Gamble et al., 1979).

Current and future attempts to reduce the standard errors, without re-deploying, are necessary to further develop discernible induced differences from fracking. Decimation of the signal down to 100 Hz has shown significant reductions in dead-band noise and increased coherency for the few stations processed in BIRRP so far. Subsampling provides two potential paths for increased estimates: more estimates of the signals of interest and a greater window-length (Simpson & Bahr, 2005). The immensity of the data has postponed further analysis due to pending deadlines. The next target is to achieve quality impedance estimates for all 40 stations and all 65 days of stimulation and recovery. These can then be used for inverse modelling and interpretation of spatial and temporal changes in three-dimensions. Occam smooth modelling is not ideal for measuring sharp-discontinuities, sharp-boundary inversion or anisotropic modelling are likely better candidates than smooth modelling. These could potential provide for a sufficient depth-constraint (Ogawa, 2002)

Implications to Microseismic Surveying

Induced deformation surveying of well-stimulations currently utilises two practices; measuring microseismic events at the surface and a down-hole array location. Down-hole bores are typically required to be within 500 m of fracturing events (Maxwell, 2014), providing for expensive monitoring analysis. Each technique provides further spatial information that the other does not, with lateral variations being more pronounced in

surface measurements and vertical in borehole data. CHECK. Results from joint mode inversion provide for knowledge on the fracture locations in 3D and implying effective hydraulic conductivity.

As electromagnetic waves are highly sensitive to fluid properties, magnetotellurics could allow for a redundancy in the need for down-hole microseismic surveying in well stimulations. Two-dimensional inversion at station 22 provide for a resistivity and dimensionality increases vertically of 300 -400 m, which is similar to the fracture front proposed from joint inversion of microseismic data (**?**). If the trends observed at other stations, show similar sensitivity to station 22, lateral constraints of layered-inversion resistivities can infer the extent of horizontal fluid migration. Inversions could replace down-hole microseismics as the provision visualising relative vertical fracture constraints. In the presence of minimal static-shifts this technique could potentially provide for quantifiable depth constraints. Maximising the informative potential of MT would utilise three-dimensional inversion routines, to provide for an extra lateral constraint. The results of 3D surveying could potentially greatly benefit well-drilling and well-production by providing three-dimensional interpretation of the regional differences of hydraulic conductivity.

CONCLUSION

Magnetotelluric approaches attempted to map the distribution of fluids associated with hydraulic fracture stimulation in the Cooper Basin. Robust signal processing produced low-quality impedance estimates for decimated samples at 500 Hz. The depth of injection and Cooper Basin resistivity have provided for difficult analysis due to noisy estimates in dead-band frequencies. At this present stage, the processed estimates of the fluid injection do not provide for sufficient analysis in the data domain or frequency domain.

Statistically adequate results from one station held reasonable estimates within dead-band frequencies. Distortion and bulk resistivity analysis has show apparent changes temporally, however without correlating the results to another station are deemed inconclusive. A previous study (Peacock et al., 2013) investigated a similar procedure with more fortuitous results. Lithological differences are deemed to be the cause of the disparity between the studies, with the high conductivity produced from the shale matrix reducing the bulk-resistive impact of an already conductive fluid. Recent attempts to enhance dead-band signal, from data decimation, have reduced dead-band estimates to below 10 % of the apparent resistivity value. Future steps similar to those provided in the paper, shall attempt to recover the electromagnetic effects shale-fracturing imposes on a region.

Acknowledgements

I would like to send my sincerest thanks to all who have helped me throughout this year. To the geophysical team at the University of Adelaide: Lars, Nigel, Dennis, Goran, Kate and Paul - thank you for you (mostly) kind words throughout the year. An incognito thank you to Jared Peacock, for all his hard work with MTpy and providing a guideline for me to follow. A special thanks is in order for Simon Carter, he has been the catalyst allowing me to race through this year without losing any hair. To Graham Heinson, for your eloquence in explaining difficult terms simply and for all the help you have provided a long the way.

Special thanks to: The Australia Geophysical Observing System (AGOS) for providing this study with financial support and for providing equipment. An enormous thank you to SANTOS also, for providing considerable financial and logistical support.

I would also like to thank the University of Adelaide, for enduring my presence for the better of 4 years and to all those friends I have met there along the way.

Lastly, I would like to thank my family for their never-ending devotion to my well-being, the family and the community.

"Pobody's Nerfect" - The Simpsons

"They are pernicious, positively pernicious, and yet I cant give them up!" - Porfiry Petrovitch (Crime and Punishment, Fyodor Dostoevsky)

REFERENCES

Ahmad, M (2014), Petrophysical and Mineralogical Evaluation of Shale Gas Reservoirs, PhD thesis.

Alexander, E.M., J.G.G. Morton, D.I. Gravestock, J. Hibburt, South Australia. Dept. of Mines, Energy. Petroleum Division & J.F. Drexel (1996), *Petroleum Geology of South Australia: Eromanga Basin*, Report book, Petroleum Division, SA Department of Mines and Energy.

Apak, S.N. (1994), *Structural Development and Control on Stratigraphy and Sedimentation in the Cooper Basin, Northeastern South Australia and Southwestern Queensland*, Univeristy of Adelaide, National Centre for Petroleum Geology and Geophysics.

Archie, GE (1942), 'The electrical resistivity log as an aid in determining some reservoir characteristics', *I. Pet Tech* **5**.

Beardsmore, Graeme (2004), 'The influence of basement on surface heat flow in the cooper basin', *Exploration Geophysics* **35**(4), 223–235.

Berdichevsky, M. N. & V. Dmitriev (1976), 'Distortion of magnetic and electric fields by near-surface later inhomogeneities', *Geophysica et Montanist* **2**(3), 447 – 483.

Bibby, H. M., T. G. Caldwell & C. Brown (2005), 'Determinable and non-determinable parameters of galvanic distortion in magnetotellurics', *Geophysical Journal International* **163**(3), 915–930.

Bierman, James, Christina Kulp & Jody Bales Foote (2011), 'Reviews of science for science librarians: Hydraulic fracturing: Geological, engineering, and environmental literature', *Science & Technology Libraries* **30**(4), 326–342.

Booker, JohnR. (2014), 'The magnetotelluric phase tensor: A critical review', *Surveys in Geophysics* **35**(1), 7–40.

Cagniard, Louis (1953), 'Basic theory of the magneto-telluric method of geophysical prospecting', *Geophysics* **18**(3), 605–635.

Caldwell, T. Grant, Hugh M. Bibby & Colin Brown (2004), 'The magnetotelluric phase tensor', *Geophysical Journal International* **158**(2), 457–469.

Chave, A.D. & A.G. Jones (2012), *The Magnetotelluric Method: Theory and Practice*, Cambridge University Press.

Chave, Alan D & David J Thomson (2003), 'A bounded influence regression estimator based on the statistics of the hat matrix', *Journal of the Royal Statistical Society: Series C (Applied Statistics)* **52**(3), 307–322.

Chave, Alan D & David J Thomson (2004), 'Bounded influence magnetotelluric response function estimation', *Geophysical Journal International* **157**(3), 988–1006.

Chave, Alan D, David J Thomson & Mark E Ander (1987), 'On the robust estimation of power spectra, coherences, and transfer functions', *Journal of Geophysical Research: Solid Earth (1978–2012)* **92**(B1), 633–648.

Cipolla, Craig L, Elyezer P Lolon, Jim C Erdle, Barry Rubin et al. (2010), 'Reservoir modeling in shale-gas reservoirs', *SPE Reservoir Evaluation & Engineering* **13**(04), 638–653.

Constable, Steven C, Robert L Parker & Catherine G Constable (1987), 'Occam's inversion: A practical algorithm for generating smooth models from electromagnetic sounding data', *Geophysics* **52**(3), 289–300.

deGroot Hedlin, Constable & S Constable (1990), 'Occam's inversion to generate smooth, two-dimensional models from magnetotelluric data', *Geophysics* **55**(12), 1613–1624.

Du, J, NR Warpinski, EJ Davis, LG Griffin & S Malone (2008), Joint inversion of downhole tiltmeter and microseismic data and its application to hydraulic fracture mapping in tight gas sand formation, *in* 'Proceeding 42nd US Rock Mechanics Symposium'.

Eisner, Leo, BJ Hulsey, Peter Duncan, Dana Jurick, Heigl Werner & William Keller (2010), 'Comparison of surface and borehole locations of induced seismicity', *Geophysical Prospecting* **58**(5), 809–820.

Fulton, SA (2012), 'Technical report: Great artesian basin resource assessment'.

Gamble, ThomasD, Wolfgang M Goubau & John Clarke (1979), 'Magnetotellurics with a remote magnetic reference', *Geophysics* **44**(1), 53–68.

Groom, Ross W & Richard C Bailey (1989), 'Decomposition of magnetotelluric impedance tensors in the presence of local three-dimensional galvanic distortion', *Journal of Geophysical Research: Solid Earth (1978–2012)* **94**(B2), 1913–1925.

Groom, RossW. & Karsten Bahr (1992), 'Corrections for near surface effects: Decomposition of the magnetotelluric impedance tensor and scaling corrections for regional resistivities: A tutorial', *Surveys in Geophysics* **13**(4-5), 341–379.

Heise, Wiebke, TG Caldwell, Hugh M Bibby & SC Bannister (2008), 'Three-dimensional modelling of magnetotelluric data from the rotokawa geothermal field, taupo volcanic zone, new zealand', *Geophysical Journal International* **173**(2), 740–750.

Hillis, Richard R, Jeremy J Meyer & Scott D Reynolds (1998), 'The australian stress map', *Exploration Geophysics* **29**(3/4), 420–427.

Hubbert, M King & David G Willis (1972), 'Mechanics of hydraulic fracturing'.

Jiracek, George R (1990), 'Near-surface and topographic distortions in electromagnetic induction', *Surveys in Geophysics* **11**(2-3), 163–203.

Jones, Alan G. & Ross W. Groom (1993), 'Strike-angle determination from the magnetotelluric impedance tensor in the presence of noise and local distortion: rotate at your peril!', *Geophysical Journal International* **113**(2), 524–534.

Khaksar, A & AB Mitchell (1995), 'An improvement in lithology interpretation from well logs in the patchawarra formation, toolachee field, cooper basin, south australia', *Exploration Geophysics* **26**(2/3), 347–353.

Krawczynski, L. (2004), *Sequence Stratigraphic Interpretation Integrated with 3-D Seismic Attribute Analysis in an Intracratonic Setting, Toolachee Formation, Cooper Basin, Australia*, Queensland University of Technology, Brisbane.

Krieger, Lars & Jared R Peacock (2014), 'Mtpy: A python toolbox for magnetotellurics', *Computers & Geosciences* **72**, 167–175.

lan Gough, D (1986), 'Seismic reflectors, conductivity, water and stress in the continental crust', *Nature* **323**, 11.

Mandl, G & RM Harkness (1987), 'Hydrocarbon migration by hydraulic fracturing', *Geological Society, London, Special Publications* **29**(1), 39–53.

Marti, A., P. Queralt & J. Ledo (2009), 'Waldim: A code for the dimensionality analysis of magnetotelluric data using the rotational invariants of the magnetotelluric tensor', *Computers & Geosciences* **35**(12), 2295 – 2303.

Marti, Anna (2014), 'The role of electrical anisotropy in magnetotelluric responses: From modelling and dimensionality analysis to inversion and interpretation', *Surveys in Geophysics* **35**(1), 179–218.

Mavromatidis, Angelos (2008), 'Two layer model of lithospheric compression and uplift/exhumation in an intracratonic setting: an example from the cooper–eromanga basins, australia', *International Journal of Earth Sciences* **97**(3), 623–634.

Maxwell, S. (2014), *Microseismic Imaging of Hydraulic Fracturing: Improved Engineering of Unconventional Shale Reservoirs*, Distinguished instructor series, SEG Books.

Maxwell, S. C., J. Rutledge, R. Jones & M. Fehler (2010), 'Petroleum reservoir characterization using downhole microseismic monitoring', *Geophysics* **75**(5), 129–137.

Meixner, Tony & Fiona Holgate (2009), 'In search of hot buried granites: a 3d map of sub-sediment granitic bodies in the cooper basin region of australia, generated from inversions of gravity data', *ASEG Extended Abstracts* **2009**(1), 1–11.

Nabighian, M.N. (1988), *Electromagnetic Methods in Applied Geophysics: Theory*, Electromagnetic Methods in Applied Geophysics, Society of Exploration Geophysics.

Nesbitt, Bruce E. (1993), 'Electrical resistivities of crustal fluids', *Journal of Geophysical Research: Solid Earth* **98**(B3), 4301–4310.

Ogawa, Yasuo (2002), 'On two-dimensional modeling of magnetotelluric field data', *Surveys in Geophysics* **23**(2-3), 251–273.

Palacky, GJ & GF West (1991), 'Electromagnetic methods in applied geophysics', *Electromagnetic methods in applied geophysics* **1**.

Parker, Robert Ladislav (1994), *Geophysical inverse theory*, Princeton university press.

Peacock, Jared R, Stephan Thiel, Graham S Heinson & Peter Reid (2013), 'Time-lapse magnetotelluric monitoring of an enhanced geothermal system', *Geophysics* **78**(3), B121–B130.

Peacock, Jared Roy, Stephan Thiel, P Reid & G Heinson (2012), 'Magnetotelluric monitoring of a fluid injection: Example from an enhanced geothermal system', *Geophysical Research Letters* **39**(18).

Pitkin, Mark Christopher, Trevor Harvey Wadham, James Milton McGowen, Warwick W Thom et al. (2012), 'Taking the first steps: Stimulating the nappamerri trough resource play'.

Revil, A, LM Cathles, S Losh & JA Nunn (1998), 'Electrical conductivity in shaly sands with geophysical applications', *Journal of Geophysical Research: Solid Earth (1978–2012)* **103**(B10), 23925–23936.

Rikitake, Tsuneji (1948), 'Notes on the electromagnetic induction within the earth'.

Rodi, William & Randall L Mackie (2001), 'Nonlinear conjugate gradients algorithm for 2-d magnetotelluric inversion', *Geophysics* **66**(1), 174–187.

Santos (2014), 'Second quarter activities report'.

Simpson, F. & K. Bahr (2005), *Practical Magnetotellurics*, Cambridge University Press.

Siripunvaraporn, Weerachai, Gary Egbert, Yongwimon Lenbury & Makoto Uyeshima (2005), 'Three-dimensional magnetotelluric inversion: data-space method', *Physics of the Earth and Planetary Interiors* **150**(1), 3–14.

Sun, Xiaowen (1997), 'Structural style of the warburton basin and control in the cooper and eromanga basins, south australia', *Exploration Geophysics* **28**(3), 333–339.

Swift Jr, Charles Moore (1967), A magnetotelluric investigation an electrical conductivity anomaly in the southwestern united states., Technical report, MASSACHUSETTS INST OF TECH CAMBRIDGE GEOPHYSICS LAB.

Valko, Peter & Michael J Economides (1995), *Hydraulic fracture mechanics*, Wiley New York, NY.

Wang, K, JM Sun, SC Geng & JL Wu (2006), 'Percolation network study of shale effects on rock electrical properties under different salinity', *Chinese Journal of Geophysics* **49**(6), 1710–1717.

Waxman, MH, LJM Smits et al. (2003), 'Electrical conductivities in oil-bearing shaly sands', *SPE Reprint Series* pp. 107–122.

Weaver, C.E. (1989), *Clays, Muds, and Shales*, Developments in Sedimentology, Elsevier Science.

Weaver, JT, AK Agarwal & FEM Lilley (2000), 'Characterization of the magnetotelluric tensor in terms of its invariants', *Geophysical Journal International* **141**(2), 321–336.

Weaver, JT, AK Agarwal & FEM Lilley (2006), 'The relationship between the magnetotelluric tensor invariants and the phase tensor of caldwell, bibby, and brown', *Exploration Geophysics* **37**(3), 261–267.

APPENDIX A: ADDITIONAL INFORMATION – PART I

Table 1: Site and their respective Cartesian co-ordinate location and the day the previewed MT stations began and terminated recording

Site	Eastings	Northings	Begin(UTC)	End(UTC)
20	425595	6897611	139	204
21	425756	6897444	139	204
22	426001	6897279	139	204
23	426106	6897073	139	204
25	426487	6896683	140	204
28	427001	6896153	138	203
40	424833	6898389	137	202
41	424699	6898553	137	202
42	424484	6898732	137	202
43	424318	6898925	137	202